

In Vivo Acoustic Super-Resolution and Super-Resolved Velocity Mapping Using Microbubbles

Kirsten Christensen-Jeffries, *Student Member, IEEE*, Richard J. Browning, *Member, IEEE*, Meng-Xing Tang, *Member, IEEE*, Christopher Dunsby, and Robert J. Eckersley, *Senior Member, IEEE*

Abstract— The structure of microvasculature cannot be resolved using standard clinical ultrasound (US) imaging frequencies due to the fundamental diffraction limit of US waves. In this work, we use a standard clinical US system to perform *in vivo* sub-diffraction imaging on a CD1, female mouse aged 8 weeks by localizing isolated US signals from bubbles flowing within the ear microvasculature, and compare our results to optical microscopy. Furthermore, we develop a new technique to map blood velocity at super-resolution by tracking individual bubbles through the vasculature. Resolution is improved from a measured lateral and axial resolution of 112 μm and 94 μm respectively in original US data, to super-resolved images of microvasculature where vessel features as fine as 19 μm are clearly visualized. Velocity maps clearly distinguish opposing flow direction and separated speed distributions in adjacent vessels, thereby enabling further differentiation between vessels otherwise not spatially separated in the image. This technique overcomes the diffraction limit to provide a non-invasive means of imaging the microvasculature at super-resolution, to depths of many centimeters. In the future, this method could non-invasively image pathological or therapeutic changes in the microvasculature at centimeter depths *in vivo*.

Index Terms— Biomedical imaging, Microbubbles, Microvasculature, Ultrasonic imaging, Ultrasound, Resolution.

Copyright (c) 2010 IEEE. Personal use of this material is permitted. Manuscript received May 22, 2014; accepted September 5, 2014.

This research was supported by the Department of Health via the National Institute for Health Research (NIHR) comprehensive Biomedical Research Center award to Guy's and St Thomas' NHS Foundation Trust in partnership with King's College London and King's College Hospital NHS Foundation Trust. The Centre of Excellence in Medical Engineering funded by the Wellcome Trust and EPSRC under grant number WT 088641/Z/09/Z. The views expressed are those of the author(s) and not necessarily those of the NHS, the NIHR or the Department of Health.

K. Christensen-Jeffries and R. J. Eckersley are with the Biomedical Engineering Department, Division of Imaging Sciences, Kings College London, London, UK (phone: 0207188837; e-mail: kirsten.christensen-jeffries@kcl.ac.uk and robert.eckersley@kcl.ac.uk).

R.J. Browning was with the Biomedical Engineering Department, Division of Imaging Sciences, Kings College London, London, UK. He is now with the Institute of Biomedical Engineering, Old Road Campus Research Building, University of Oxford, Oxford, OX3 7DQ, UK (email: richard.browning@eng.ox.ac.uk).

C. Dunsby is with the Department of Physics Imperial College London, London, SW7 2AZ, UK and the Centre for Histopathology, Imperial College London, London, W12 0NN, UK (email: christopher.dunsby@imperial.ac.uk).

M. X. Tang is with the Department of Bioengineering, Imperial College London, London, SW7 2AZ, UK (email: mengxing.tang@imperial.ac.uk).

I. INTRODUCTION

The diffraction-limited image resolution inherent to conventional US is unable to adequately resolve the microvasculature. Many microvascular diseases, such as those associated with diabetes [1] and coronary heart disease [2], exhibit architectural changes in the microvascular structure, as well as variations in vascular flow. Angiogenesis, the formation of new blood vessels from existing vasculature, also plays a vital role in the development of many pathologies, including the growth and metastasis of tumors, and is an important predictor of the biological behavior of certain cancers [3]. The microcirculation can also be an active site of blood flow control and metabolic activity, where variations in vascular blood flow can be indicative of conditions such as ischemia, malignancies and diabetes-related microvascular diseases [4]. Assessment of early changes in the microvasculature using US would allow early clinical intervention and a non-invasive means of monitoring the treatment of such diseases [5]–[6].

Currently, visualization of the vasculature in clinical US can be achieved using microbubble contrast agents [7]–[10]. These are gas filled spheres of a few micrometers in size. They exhibit a large backscatter signal as their resonance frequency matches the 1 to 15 MHz range of clinical US and generally they do not extravasate, which makes them an ideal vascular contrast agent [8]. Progress has been made to image the vasculature using contrast agents with techniques such as maximum intensity persistence imaging [9] and power Doppler sonography [10] allowing detection of blood flow. However, the fundamental limitation on US resolution by diffraction of the transmitted and received waves means imaging at the micrometer scale is still required. High frequency US has been developed as a means of obtaining high-resolution imaging [11], however these techniques have limited application due to the inherent compromise between higher frequencies and limited penetration depth.

Since microbubbles are considerably smaller than the US resolution limit, they can be considered as point scatterers in the acoustic field and their image is blurred by the point spread function (PSF) of the imaging system [12]. Sub-diffraction imaging is a well-developed field in optical microscopy [13]–[16], where methods have been developed to

overcome the same fundamental physics through the localization of many spatially isolated photo-activatable fluorophore signals. Initial *in vitro* work by ourselves [17] and others [18], have demonstrated the potential for microbubbles to be used in a similar way to achieve sub-diffraction US imaging at depths of up to 4 cm in phantoms. In this paper we present the use of this super-resolution technique *in vivo*. This uses an unmodified clinical US system in a standard contrast enhanced mode. In addition, since this technique utilizes microbubble contrast agents that have an intravascular rheology similar to that of red blood cells [19], we create a new technique to map blood velocity at super-resolution. For comparison, optical images as well as conventional contrast enhanced US images are displayed alongside the super-resolved images.

II. MATERIALS AND METHODS

A. Ultrasound Equipment and Acquisition

All data was acquired using a standard, unmodified Siemens Acuson Sequoia clinical US scanning system (Siemens, Issaquah, WA) using Cadence™ contrast pulse sequencing (CPS) mode [20]. This is a standard US imaging mode that is sensitive and specific to contrast agents based on the processing of receive signals to emphasize nonlinear bubble signals, while suppressing the linear contribution where tissue is predominant. A 15L8 linear array transducer was chosen for use in this experiment due to the suitability of a small probe size to the *in vivo* mouse ear model. This was used at an average transmit frequency of 6.5 MHz and a low transmit power equivalent to a mechanical index of 0.16. Data was acquired using the maximum frame rate and dynamic range settings available for this system of 25 Hz and 100 dB respectively.

B. Ultrasound System Characterization

Characterization of the PSF was performed to assess the diffraction limited resolution and localization precision of the US imaging system under ideal conditions. A 100 μm diameter brass wire was held horizontally between two fixings in a gas equilibrated water bath. The wire was positioned normal to the US image plane so that the cross-section of the wire was imaged to imitate a point scatterer. This was performed at depths of 0.5 cm, 0.75 cm, 1 cm and 1.25 cm from the transducer face to test the PSF over the range of depths imaged *in vivo*. Firstly, each frame was de-compressed to remove the logarithmic image scaling applied by the scanner acquisition software. The center of mass of the wire signal was then calculated for each frame, as well as the full width half maximum (FWHM) of the signal in the lateral and axial directions. The resolution of the US system was measured as the average FWHM over 100 frames in lateral and axial directions. The localization precision was measured to be the standard deviation of the measured center of mass over 100 frames.

To account for the finite size of the wire in the measurement

of the PSF we de-convolved the measured FWHM value by the finite size of the wire to obtain new values of the PSF FWHM. De-convolving, this becomes:

$$FWHMx_{measured}^2 = FWHMx_{actual}^2 + FWHMx_{PSF}^2 \quad (1)$$

$$FWHMx_{PSF} = \sqrt{FWHMx_{measured}^2 - FWHMx_{actual}^2} \quad (2)$$

C. In Vivo Model

All animal work was conducted under the authority of the UK Home Office project license as required by the Animals (Scientific Procedures) Act 1986. Mice were maintained in a minimal disease facility fully compliant with Home Office guidelines with food and water *ad libitum*. A 27 g, 8-week-old, female, CD1 mouse was anaesthetized using isoflurane gas and monitored constantly.

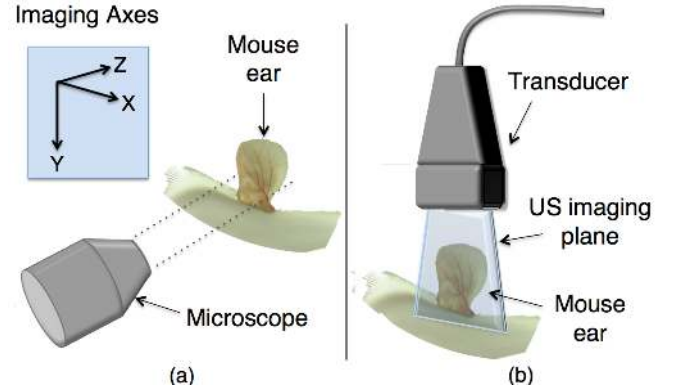


Fig. 1. Schematic diagram of imaging set-up. (a) Optical set-up where microscopic imaging was performed across the surface of the mouse ear. (b) US set-up consisting of the transducer positioned above the mouse ear such that the entire width was within the US lateral field of view.

D. Optical Imaging

One ear of the mouse was depilated by shaving and depilatory cream was applied to ensure visibility of the vascular structure for optical microscopy. The mouse was positioned on a light diffusing stage such that the ear was relatively flat against the surface of the stage (Fig. 1(a)). Optical images of the vascular structure were then acquired using a Wild Heerbrugg M650 (Switzerland) microscope and a SONY Handycam HDR SR12E (Japan) camera.

E. Ultrasound Imaging

The anaesthetized mouse was transferred to a heat mat and positioned with the prepared ear vertical to the surface, as shown in Fig. 1(b). The transducer was positioned above the

ear such that the entire width of the ear was within the lateral field of view and the length of the ear extended in the axial imaging direction. US gel was applied around the ear to cover the entire elevational imaging plane as well as to flatten the ear within the plane, and was applied above the ear in order to couple to the imaging device.

A heparin flushed, 29G catheter was placed in the mouse tail vein. A suspension of SonoVue (Bracco Imaging SpA, Milan, Italy) microbubbles at 2.5× original concentration of original vial was administered using a syringe pump with an infusion rate of between 0.2-5.0 μl per minute to provide a bubble per frame density which ensured that a high proportion of the bubble signals in each frame were spatially isolated. The infusion rate was varied in response to visual inspection of the images in real time. An estimate suggests that the resulting bubble infusion rate per unit blood volume is in the range of ~1-10 times that used in conventional human contrast imaging [21] - [22]. The total injected volume did not exceed 200 μl . The region around the mouse ear was defined on the US system at a depth of 0.6-1.5 cm and video data of microbubbles flowing through branching blood vessels in the mouse ear was captured directly to PC from the S-Video out via an analogue to digital capture device (Intensity Shuttle, Blackmagic Design). As a consequence, the frame rate of the acquired video sequence was limited to 25 fps. However, storage capacity was not restricted by the limited onboard hardware of the ultrasound system. Upon reaching the maximum injection volume, the anaesthetized mouse was culled.

F. Microbubble Localization

Algorithms were written in MATLAB (The MathWorks, Inc., Natick, MA) to process the acquired video data as follows. Firstly, all raw image frames were logarithmically decompressed. Then a region containing a constant scatter signal from the base of the ear was identified within a reference frame. The cross correlation of this region was then calculated between the reference frame and all subsequent frames in order to identify inter-frame motion. Breathing induced motion artifacts were then removed by excluding frames with an empirically determined cross-correlation value of less than 0.98. The remaining frames were then processed based on our previous work [17], where firstly frames which potentially contained a microbubble signal were identified by comparing the total intensity of the frame to an empirically determined threshold based on the characterization of the noise of the system. ‘Empty’ frames were added to a rolling background average, whereas potential bubble frames had the rolling background average subtracted from them. The rolling average was taken over $n = 10$ frames in order to remove the unwanted background signals due to static structures without removing slow moving bubbles. Potential bubble frames were then binarized using an intensity threshold, and the size of any connected regions in the image were compared to the expected PSF based on our initial characterization experiments in order to reject signals coming from noise or from multiple bubbles.

This is because we cannot assume that the center of mass of signals from multiple separated unresolved microbubbles within a PSF sized volume are representative of the bubble location. The intensity-weighted center of mass of each spatially isolated microbubble signal was then calculated to obtain coordinates for the localized bubble position C_x, C_y .

G. Super-Resolution Image Generation

A script was written for generation of the final super-resolution image. Here, each individual bubble localization was represented by a 2-D Gaussian profile centered at C_x, C_y with standard deviations, σ_x and σ_y , given by the average lateral and axial localization uncertainty of the PSF FWHM. The super-resolution map resulting from the sum of all the individual centroid localization distributions across all frames creates an image in which the displayed value is proportional to the chance of finding a microbubble positioned at that location.

H. Microbubble Tracking

Microbubble tracking algorithms were written in MATLAB to determine the flow velocity within the microvasculature. Firstly, microbubble signals deemed to be spatially isolated were identified in each frame as described in the microbubble localization program. For each frame n , individual microbubble signals were identified. The individual intensity cross correlations between each bubble signal in frame n and each of the bubble signals found in frame $n-1$ within a 400 micrometer search window were then calculated and the maximum cross correlation was found for each signal in frame n . The search window size was defined to reject bubbles which far exceeded the expected red blood cell velocity in the ear [19]. A pair of signals were deemed to come from the same bubble if the maximum cross correlation exceeded an empirically determined threshold of 0.8. For each pair, a velocity vector was then calculated between C_x^n, C_y^n and C_x^{n-1}, C_y^{n-1} and assigned to the centroid location C_x^n, C_y^n in frame n .

I. Flow Velocity Image Generation

To generate flow velocity images, the velocity vectors v_i associated with each localized bubble position $C = (C_x, C_y)$ are combined using a weighted spatial averaging approach. Firstly, for each velocity vector v_c at C , all j centroids which exist within a neighborhood of radius $r = 40 \mu\text{m}$ are identified. A weighting w_i is then applied to each v_i , given by

$$w_i = e^{-\left(\frac{d_i}{r}\right)^2} \quad (3)$$

where d_i is the distance from C to centroid C_i . The velocity v_c is then given by the weighted sum of all neighborhood velocity distributions

$$v_c = \frac{1}{Z} \sum_{i=1}^j w_i v_i, \quad (4)$$

where Z is the normalization factor given by

$$Z = \sum_{i=1}^j w_i. \quad (5)$$

The speed and direction components of velocity are then presented in separate images. Velocity vector components for each localization were displayed on the 95% confidence interval of the 2D Gaussian profile used to generate the super-resolved images. In this way, noise present in the velocity data is reduced, while the underlying bubble positions are still localized to within the localization precision of the system.

III. RESULTS

To estimate the diffraction limited resolution under ideal conditions, we used a stationary point scatterer to measure the system PSF FWHM over the depth range 0.5-1.25 cm. As the backscatter from the scatterer was very strong we used a low gain and no additional TGC, hence the background noise is below the quantization level of the digitizer.

Fig. 2 shows an example image of the wire cross-section at a depth of 1.25 cm, which provides the highest measured resolution for CPS imaging over the range investigated. Here, the resolution was measured to be a FWHM of 112 μm in the lateral and 94 μm in the axial direction. The localization precision of this point scatterer in the lateral and axial directions was found to be 6 and 2 μm respectively.

These results compare well with the estimated theoretical

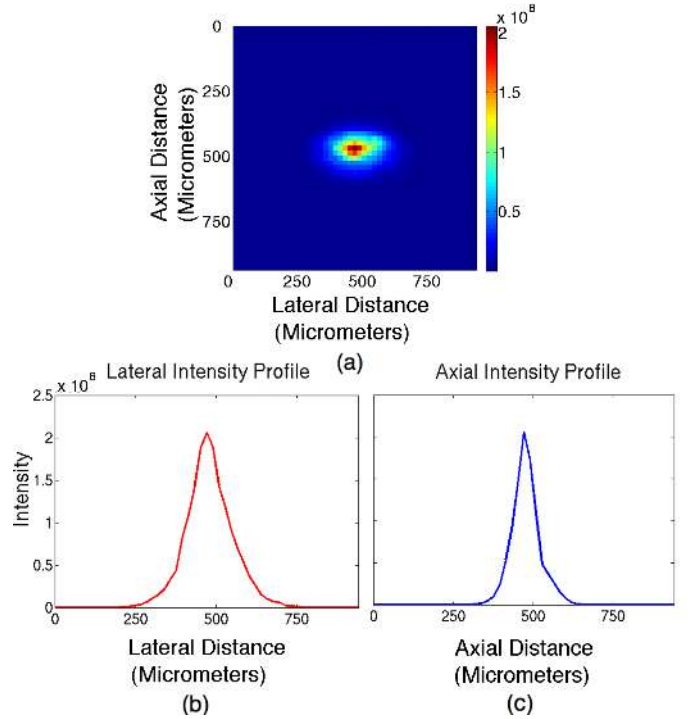


Fig. 2. Characterization of US imaging system. (a) shows an example logarithmically decompressed image of 100 μm diameter wire target cross-section at 1.25 cm. (b) and (c) display example FWHMs in the lateral and axial directions respectively.

resolution. Given that we are using CPS imaging, we assume that the effective US frequency is the mean of the fundamental and second harmonic, i.e. 9.75 MHz. Axially, this gives the FWHM of the spatial pulse length to be 80 μm .

The expected lateral resolution is harder to estimate in the absence of proprietary knowledge of the exact transducer design - assuming a F/1 aperture gives a FWHM of 160 μm .

Fig. 3(a) shows a typical CPS image frame of the mouse ear

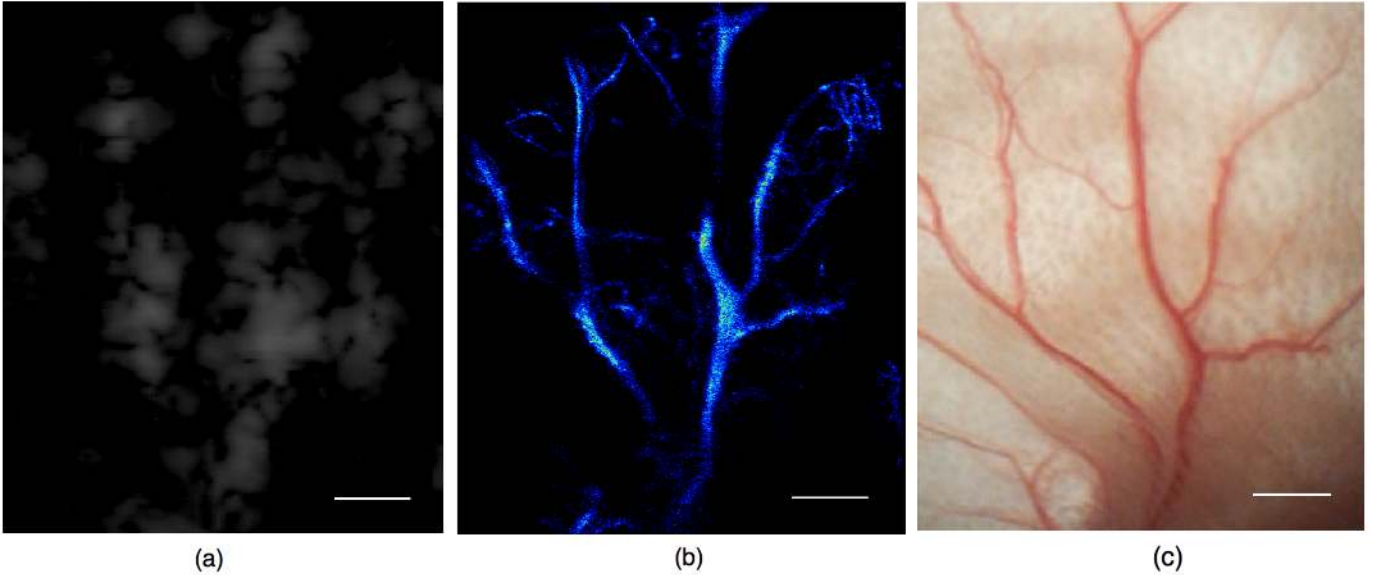


Fig. 3. Comparative images of mouse ear microvasculature using standard contrast enhanced US, single bubble localization method, and optical microscopy obtained using a surgical microscope. (a) A single high microbubble concentration image frame acquired using conventional Cadence™ CPS imaging mode. (b) Super-resolution image created as a probability density map where brightness represents the number of bubbles localized in a given location. (c) Corresponding optical image of the vasculature within the same mouse ear acquired *in vivo*. Scale bars, 1 mm.

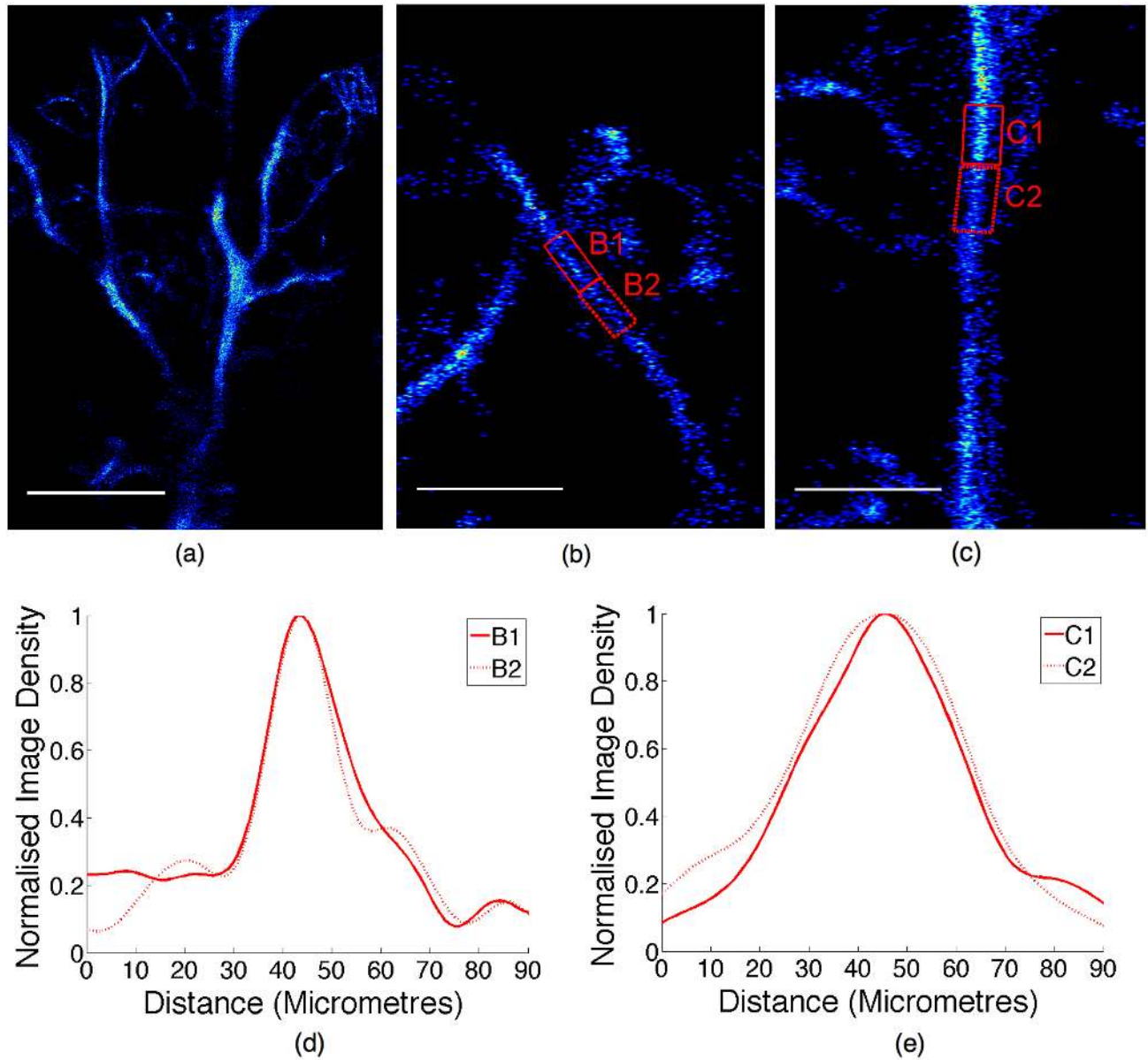


Fig. 4. Super-resolved vessel measurements. (a) Super-resolution image as shown in Fig. 3B, where the white boxes identify two vessels of interest, shown at higher magnification (b) and (c). Fig 4(d) and (e) show two average normalized line profiles across regions of 200 μm length (B1-B2 and C1-C2), as outlined in (b) and (c). The mean profile FWHM was $19 \pm 2.8 \mu\text{m}$ and $39 \pm 1.4 \mu\text{m}$ for the curves shown in (d) and (e) respectively. Scale bars, 2 mm (a), 500 μm (b, c).

vasculature containing multiple bubble signals which are not spatially isolated – leading to an image that is similar to conventional contrast imaging. Here, diffraction limits visibility of the underlying structure and makes size estimation of the vessels impossible and the bubble concentration is too high to allow individual bubbles to be localized. Fig. 3(b) displays the super-resolved *in vivo* image produced using single bubble localization, where the branching vessel structures in the mouse ear are clearly visible across the entire imaging depth down to 1.5 cm. An optical image of the vascular structure in the mouse ear is shown in Fig. 3(c), where the vessel structure corresponds well to that visualized using our technique.

To illustrate this, vessels were identified in the super-resolution image as shown in Fig. 4(a), and shown at higher magnification in Fig. 4(b) and (c). Average vessel diameters of

$19 \pm 2.8 \mu\text{m}$ (Fig. 4(d)), and $39 \pm 1.4 \mu\text{m}$ (Fig. 4(e)) were measured at a depth of 0.8 cm and 0.9 cm respectively, compared to the measured diffraction limited lateral and axial resolutions of 112 μm and 94 μm . Corresponding measurements from an optical image for the vessel analyzed in Fig. 4(d) give an average vessel diameter of $24.4 \pm 4.8 \mu\text{m}$ which is in good agreement to that measured using single bubble localization (Fig. 5).

Fig. 6(a) shows the original super-resolution image, alongside color-encoded flow images of the vascular structure attained at super-resolution (Fig. 4(b) and (c)). Fig. 6(b) displays the directional component of velocity over 360° and Fig. 6(c) shows the speed variation for bubble flow within the vessels.

Differentiation between flow direction and speed can separate the opposing blood flow into arteries and veins, and therefore enhance the visualization of objects within the image

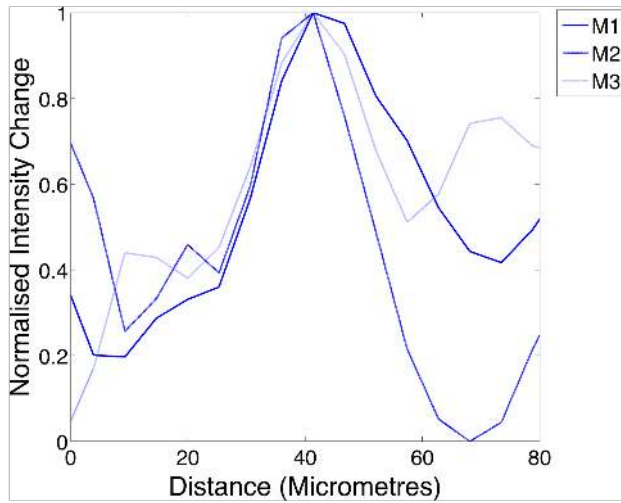


Fig. 5. Optical image profiles at 3 locations (M1-M3) across vessel shown in Fig. 4(b) and corresponding profiles in Fig. 4(d), where each profile spans 200 μm of the length of the vessel. The mean FWHM of the optical profiles is $24.4 \pm 4.8 \mu\text{m}$. The pixel size of the optical images is $5.4 \mu\text{m}$.

which are not otherwise spatially separable.

Fig. 7 shows one such example in more detail, where opposing flow directions (Fig. 7(a)) can be seen to correlate with two distinct speed distributions (Fig. 7(b)). This is shown in the speed profile along a 400 μm section of the vessel structure (Fig. 7(b)), which reveals a high speed at the vessel centers with decreasing speeds toward the vessel walls (Fig. 7(c)). The peak average velocity in the artery is $3080 \mu\text{m/s}$, and only $1850 \mu\text{m/s}$ in the vein. This higher speed arterial flow and slower flow present in veins can be observed throughout the vasculature (Fig. 8).

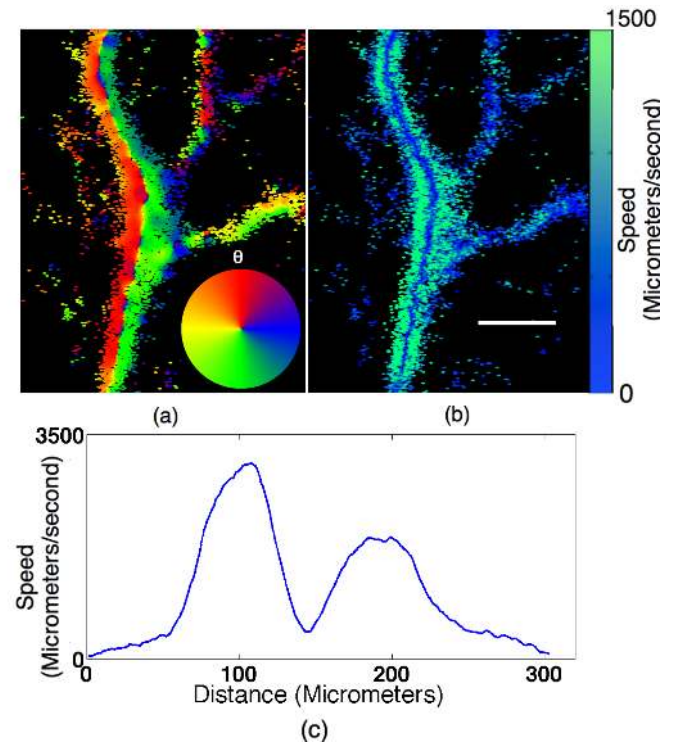


Fig. 7. Regional velocity maps. (a) Magnified image section from Fig. 6B where what appeared initially to be one vessel can be differentiated into an adjacent artery and vein with opposing flows. (b) shows the corresponding speed of flow through the vessels, where speeds above $1500 \mu\text{m/s}$ are set to the maximum on the colorbar. The corresponding average flow profile over $400 \mu\text{m}$ (white box) is shown in (c). In both, two vessel profiles can be clearly identified by a distinct slow flow separation, where faster flow is apparent in the centers of the vessels. Scale bar, $500 \mu\text{m}$.

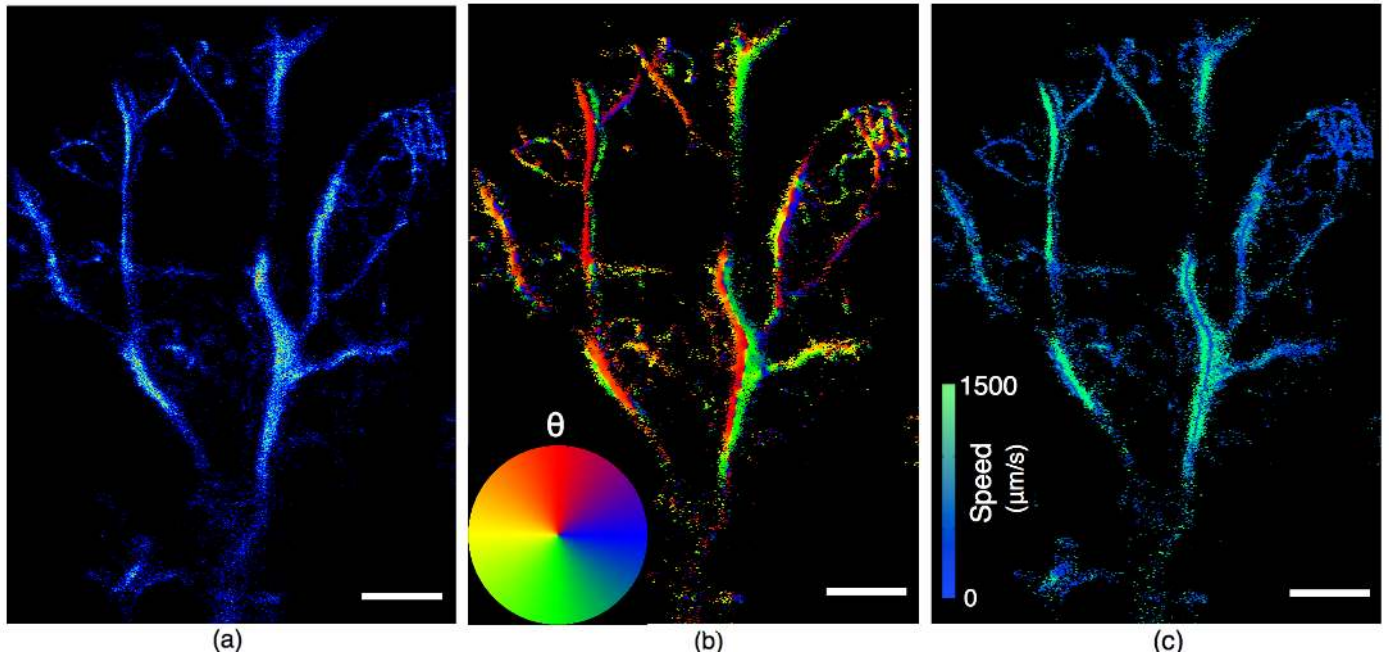


Fig. 6. Super-resolution velocity maps. (a) Super-resolution image as shown in Fig. 3(b), and corresponding image displaying the direction of blood flow is shown in (b). (c) shows the corresponding speed of flow through the vessels, where speeds above $1500 \mu\text{m/s}$ are set to the maximum on the colorbar. Scale bars, 1 mm .

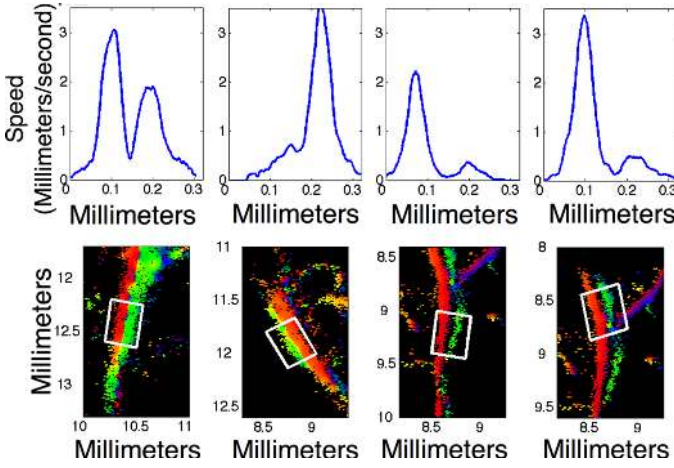


Fig. 8. Magnified image sections taken throughout the microvasculature from Fig. 6(b), showing vessels with opposing flow directions, and their corresponding average flow speed profiles across 400 μm (indicated by the white boxes).

IV. DISCUSSION

Using conventional CPS contrast imaging, the mouse vasculature cannot be observed since the branching structures are significantly smaller than even the optimal system PSF FWHM. However, by detecting and deconvolving spatially isolated scattering events and superimposing all the localized bubble positions onto a single map, vessel structures over 5-times smaller than the optimal diffraction limited resolution were resolved.

Some vessels appear more clearly in the super-resolution US image than in the optical image, and vice versa. Since the number of localizations in the super-resolution image is proportional to the likelihood of a bubble being present over the course of the observation, the concentration of microbubbles in the vessels dictates their visualization in the final image. In addition, variations in the position of the mouse ear in the elevational direction may cause some vessels to move out of the plane imaged by the US system. While we tried to ensure that the mouse ear was as flat as possible for both the optical and US imaging, the inherent differences between the two modalities mean that there will inevitably be some discrepancies between the two, i.e. small vessels on the far side of the ear from the surgical microscope used to acquire the optical image will not be clearly resolved. This is a limitation of the 2-D acquisition process and in the future, a 3-D implementation of this technique will allow complex structures to be super-resolved in the elevational plane.

A recent imaging technique called photo-acoustic tomography (PAT) has been developed which detects the acoustic waves generated from an object by optical absorption after being irradiated with pulsed or intensity modulated optical waves. This technique, and embodiments of it such as photo-acoustic microscopy (PAM), photo-acoustic computed tomography (PACT) and photo-acoustic endoscopy (PAE) have shown impressive 3-D renderings of microvascular structures *in vivo* [23]. This technique, however, suffers from the inherent compromise between achievable spatial resolution

and depth penetration, with estimated optimal resolutions for optical resolution PAM (OR-PAM) of 5 μm laterally and 15 μm axially, but with a limit of 0.7 mm penetration depth [24]. This can be improved to a depth of 50 mm with ultrasound array based PACT (UA-PACT), but with a considerable reduction in the achievable resolution to 800 μm laterally and 300 μm axially [23], [25]-[26].

Moreover, the technology has not yet been translated to the clinic and will require specialized equipment to enable this transition [23]. Our super-resolution technique detects microvasculature with a resolution of under 20 μm at imaging depths of > 1 cm and has been performed using standard equipment routinely used in clinical US scans, requiring only the image data. Microbubbles are approved for clinical use worldwide, and although not used routinely for clinical US scans, their use as a contrast imaging agent in diagnostics and therapeutics is continuing to grow.

There are two main factors which influence the visualization of the vasculature in the final super-resolution images. Firstly, the spatial resolution is limited by the localization uncertainties σ_x and σ_y of the system since this determines the size of each Gaussian localization profile. Secondly, the density of localizations in the final image determines the signal to noise ratio in the rendered image. A reduced localization density gives less complete information about the spatial distribution of the bubble flow inside the structure.

A fundamental compromise therefore exists between the exclusion criteria of bubble signals and the density of localizations in the final image. The strict inclusion of bubbles with only a narrow spectrum of sizes and intensities similar to that of our expected PSF should result in a sharper image with a higher resolution. However, the spatial distribution of localizations will be more sparse unless acquisition time or frame rate is increased. These are therefore key parameters for optimizing the performance of this technique in the future.

The microbubble localization imaging approach requires that the microbubbles sample the entire microvascular structure. Therefore, increasing the detection frame rate will increase the microbubble localization density per second. However, if the flow rate in a particular vessel is sufficiently slow that a microbubble moves by less than the localization precision between frames, then no additional information is gained by further increasing the frame rate. Therefore, for optimal data collection, the US frame rate must be chosen according to the localization precision and the maximum microbubble velocity expected for a given sample. Currently, our processing algorithms can process up to 13 frames per second. In the future, optimization of our current processing algorithms will enable localizations to be plotted in each frame, and thus the final image to be built up in real time at higher frame rates. This technique would benefit from the development of automated or semi-automated processing which is consistent across patients.

One possible modification of the technique may involve the use of mono-dispersed bubbles. These will have the same

fundamental frequency and should respond in a similar way to a specific ultrasound wave. Backscatter signals depend on the mechanical response of the bubble and the point spread function of the imaging system and should therefore be more uniform with a mono-dispersed bubble solution. However, due to a spatially variant PSF, there will still be some variation in signals across the field of view.

The resolution of this technique is fundamentally limited by the achievable PSF localization precision; our characterization measurements suggest that this is 2 to 6 μm for the system used. The data acquired to achieve this super-resolution is the processed image output from a standard, unmodified clinical ultrasound system; this has been digitally and logarithmically compressed, as well as envelope detected by the system. Each of these processes could reduce the achievable precision. Using raw data, the read-out noise of the system would be the fundamental limit on localization precision of the US system.

The localization algorithm employed may reject signals from bubble-wall interactions as they may not match the expected PSF. In future work we plan to use an optical microscope in combination with our acoustic set-up to optically visualize and acoustically locate the bubbles in a tube phantom; this will provide further insight into bubble interactions and velocities.

The distribution of microbubble localization events is indicative of the concentration of microbubbles throughout the vessel, regardless of the flow profile. Coupled arteries and veins that are touching will have no spatial separation in super-resolved localization density maps, but can be distinguished by mapping the velocity. This has been shown in Fig. 8, where both speed profiles and bubble direction maps display a clear distinction between coupled vessels, with a clear dip in speed between vessels with opposing flow. This speed does not reduce to zero in any of the cases analyzed here. This could be due to a number of factors. First, speed and velocity vectors were associated with the 95% confidence interval around their localized position. Therefore, overlapping velocity vectors will likely be non-zero on average since only few microbubbles are included in each estimate. Secondly, the spatial averaging of the velocity vectors means that unless the bubbles in opposing vessels were travelling at exactly the opposite velocity in magnitude and direction, the overall average speed component will be non-zero. For example, the two vessels may not run precisely in parallel.

The extension of this technique to extract flow velocity data from bubble localizations widens the application of the technique to include those of Doppler imaging, with the significant advantage of having flow information at super-resolution. Direction and speed images provide a higher level of information to the already super-resolved structures, enabling visualization of even smaller structures, and dynamics within the vessels. The potential to non-invasively image the microvascular flow deep within the body with US has widespread implications for the detection, diagnosis and management of many diseases. For example, neovascularization and red blood cell velocity changes, which

can be indicative of early stage ischemia, tumor growth and wide ranging vascular diseases [4], [27].

V. CONCLUSION

Our results demonstrate that single bubble localization can produce acoustic super-resolution and super-resolved flow velocity images *in vivo* from standard image data acquired by an unmodified clinical US system using simple post-processing localization algorithms. This approach can be applied to achieve an enhanced spatial resolution for US systems operating at any transmit and/or receive frequency. With the development of existing motion correction techniques, e.g. [28]–[29], as well as fast 3-D US acquisition [30], this technique has the potential to greatly enhance the resolution achieved when imaging vasculature deep within the body.

AUTHOR CONTRIBUTIONS

All authors contributed extensively to this work and wrote the manuscript. K. Christensen-Jeffries, R. J. Browning and R. J. Eckersley designed the experiment. K. Christensen-Jeffries and R. J. Browning performed the experiment. C. Dunsby, M. X. Tang, and R. J. Eckersley developed the initial concept and contributed equally to work.

ACKNOWLEDGMENTS

The authors thank Kavitha Sunassee and Stephen Clark for assistance with the *in vivo* animal work and James Clark for use of microscope equipment.

REFERENCES

- [1] R. Zatz, B. M. Brenner, "Pathogenesis of diabetic microangiopathy. The hemodynamic view," *Am. J. Med.*, vol. 80, no.3, pp. 443–453, 1986.
- [2] P. G. Camici, F. Crea, "Coronary microvascular dysfunction," *New. Engl. J. Med.*, vol. 356, pp. 830–840, 2007.
- [3] P. Carmeliet, R. K. Jain, "Angiogenesis in cancer and other diseases," *Nature*, vol. 407, no. 6801, pp. 249–257, 2000.
- [4] W. T. Cade, "Diabetes-Related Microvascular and Macrovascular Diseases in the Physical Therapy Setting," *Phys. Ther.*, vol. 88, no.11, pp. 1322–1335, 2008.
- [5] D. M. McDonald, P. L. Choyke, "Imaging of angiogenesis: from microscope to clinic," *Nat. Med.*, vol. 9, pp. 713–725, 2003.
- [6] K. Wei, "Contrast Echocardiography: Applications and Limitations," *Cardiol. Rev.*, vol. 20, no. 1, pp. 25–32, 2012.
- [7] D. Cosgrove, N. Lassau, "Imaging of perfusion using ultrasound," *N. Eur. J. Nucl. Med. Mol. Imaging.*, vol. 37, no. 1 pp. S65–S85, 2010.
- [8] H. Becher, P. N. Burns, "Contrast Agents for Ultrasound," in *Handbook of Contrast Echocardiography*, Berlin, Germany: Springer-Verlag, 2000, ch.1, sec. 2, pp. 5–16.
- [9] M. A. Pysz *et al.*, "Assessment and monitoring tumor vascularity with contrast-enhanced ultrasound maximum intensity persistence imaging," *Invest. Radiol.*, vol. 46, no. 3, pp. 187–95, 2011.
- [10] H. Paitleitner, H. Steiner, G. Hasenoechl, A. Staudach, "Three-dimensional power Doppler sonography: imaging and quantifying blood flow and vascularization," *Ultrasound. Obstet. Gynecol.*, vol. 14, no. 2, pp. 139–43, 1999.
- [11] G. R. Lockwood, D. H. Turnbull, D.A. Christopher, F.S. Foster, "Beyond 30 MHz [applications of high-frequency ultrasound imaging]," *IEEE. Eng. Med. Biol.*, vol. 15, no. 6 pp. 60 – 71, 1996.
- [12] T. L. Szabo, "Wave Scattering and Imaging" in *Diagnostic Ultrasound Imaging: Inside out*, 2nd ed. Boston: Elsevier Academic Press, 2004, pp. 213–242.

- [13] E. Betzig *et al.*, "Imaging intracellular fluorescent proteins at nanometer resolution," *Science*, vol. 313, no. 5793, pp. 1642-1645, 2006.
- [14] M. J. Rust, M. Bates, X. Zhuang, "Sub-diffraction-limit imaging by stochastic optical reconstruction microscopy (STORM)," *Nature Methods*, vol. 3, no. 10, pp. 793-796, 2006.
- [15] S. T. Hess, T. P. K. Girirajan, M. D. Mason, "Ultra-High Resolution Imaging by Fluorescence Photoactivation Localization Microscopy," *Biophys. J.*, vol. 91, no. 11, pp. 4258-4272, 2006.
- [16] M. Bates, B. Huang, G. T. Dempsey, X. Zhuang, "Multicolor super-resolution imaging with photo-switchable fluorescent probes," *Science*, vol. 317, no. 5845, pp. 1749-1753, 2007.
- [17] O. M. Viessmann, R. J. Eckersley, K. Christensen-Jeffries, M. X. Tang, C. Dunsby, "Acoustic super-resolution with ultrasound and microbubbles," *Phys. Med. Biol.*, vol. 58, no. 18, pp. 6447-6458, 2013.
- [18] Y. Desailly, O. Couture, M. Fink, M. Tanter, "Sono-activated ultrasound localization microscopy," *Appl. Phys. Lett.*, vol. 103, no. 17, pp. 174107, 2013.
- [19] J. H. Barker *et al.*, "The hairless mouse ear for in vivo studies of skin microcirculation," *Plast. Reconstr. Surg.*, vol. 83, no. 6, pp. 948-59, 1989.
- [20] P. J. Phillips, "Contrast pulse sequences (CPS): imaging nonlinear microbubbles," *Proc. IEEE Ultrason. Symp.*, vol. 2, pp. 1739-1745, 2001.
- [21] C. Greis, "Technology overview: SonoVue (Bracco, Milan)," *Eur. Radiol. Suppl.*, vol. 14, Suppl. 8, pp. 11-15, (2004).
- [22] A. Saracco *et al.*, "Bolus compared with continuous infusion of microbubble contrast agent using real-time contrast harmonic imaging ultrasound in breast tumors", *Acta. Radiol.*, vol. 50, no. 8, pp. 854-859, 2009.
- [23] S. Hu, L. V. Wang, "Photoacoustic imaging and characterization of the microvasculature," *J. Biomed. Opt.*, vol. 15, no.1, 011101, Jan-Feb. 2010.
- [24] K. Maslov, H. F. Zhang, S. Hu, L.V. Wang, "Optical-resolution photoacoustic microscopy for *in vivo* imaging of single capillaries," *Opt. Lett.*, vol. 33, no. 9, pp. 929-931, 2008.
- [25] G. Ku, L. V. Wang, "Deeply penetrating photoacoustic tomography in biological tissues enhanced with an optical contrast agent" *Opt. Lett.*, vol. 30, no. 5, pp. 507-509, 2005.
- [26] L. Song, R. Bitton, L. V. Wang, K. K. Shung, K. Maslov, "Fast 3-d dark field reflection- mode photoacoustic microscopy in vivo with a 30 MHz ultrasound linear array", *J. Biomed. Opt.* vol. 13, no. 8, 054028, 2008.
- [27] S. Kaul, H. Ito, "Review: Clinical Cardiology: New Frontiers: Microvasculature in Acute Myocardial Ischemia: Part I: Evolving Concepts in Pathophysiology, Diagnosis, and Treatment," *Circulation*, vol. 109, pp. 146-149, 2004.
- [28] M.G. Strintzis, I. Kokkinidi, "Maximum likelihood motion estimation in ultrasound image sequences," *IEEE Signal Process. Lett.*, vol. 4, no. 6, pp. 1156-1157, 1997.
- [29] F. Yeung, S.F. Levinson, K.J. Parker, "Multilevel and motion model-based ultrasonic speckle tracking algorithms," *Ultrasound Med. Biol.*, vol. 24, no. 3, pp. 427-441, 1998.
- [30] O. Couture, M. Fink, and M. Tanter, "Ultrasound contrast plane wave imaging," *IEEE Trans. Ultrason. Ferroelectr. Freq. Control*, vol. 59, no. 12, pp. 2676-2683, 2012.